Efficient photocatalytic water-splitting performance by ternary CdS/Pt-N-TiO₂ and CdS/Pt-N,F-TiO₂: Interplay between CdS photo corrosion and TiO₂-dopping

M. Solakidou[a], A. Giannakas[b], Y. Georgiou[a], N. Boukos[c], M. Louloudi[a], Y. Deligiannakis[d],*

[a] Laboratory of Biomimetic Catalysis and Hybrid Materials, Department of Chemistry, University of Ioannina,GR45110, Ioannina, Greece
[b] Department of Business Administration of Agricultural and Food Enterprises, University of Patras, G. Seferi 2, GR30100, Agrinio, Greece
[c] Institute of Nanoscience and Nanotechnology, National Centre for Scientific Research "Demokritos" Patriarchou Grigoriou E' & Neapoleos, Str. GR15310, Agia Paraskevi, Attikis, Greece
[d] Laboratory of Physical Chemistry of Materials and Environment, Department of Physics, University of Ioannina, GR45110, Ioannina, Greece

ARTICLE INFO

ABSTRACT

22Z-Scheme CdS/Pt-N-TiO₂ and CdS/Pt-N,FTiO₂ nanocatalysts were synthesized using a sol – gel impregnation method and evaluated for their photocatalytic H₂/O₂ production *via* overall water splitting, with no extrrenal electron or hole acceptors. The 0.5CdS/Pt-N-TiO₂ material achieved a photocatlytic production of 639 μmol/g/h of H₂ in tandem with 319 μmol/g/h of O₂. The photocatalytic H₂/O₂ production data show that N-incorporation in the TiO₂ lattice boosts overall water splitting, while F-incorporation inhibits the catalytic performance. Quantitative monitoring of the photogenerated Ti³⁺-surface and Ti³⁺-lattice electrons, as well as of the photogenerated holes (h⁺) by Electron Parmagnetic Resonce spectrsocopy, show that CdS/Pt-N-TiO₂ achieves enhanced e⁻/h⁺ photogeneration due to intraband states generated by N-dopping, facilitating the flow of electrons *via* Pt to the valence band of CdS. The leaching of Cd²⁺ ions' due to phootocorrosion of the CdS quantum dots, was montiored *in-situ* using Anodic StrippingVoltammtery (ASV). The Cd²⁺ leaching data reveal a severe inhibition of CdS photocorrosion ofN-dopped catalysts, CdS/Pt-N-TiO₂. This reveals a dual beneficial role of N-atoms: [i] boosting the visible light photocactivity, and [ii] inhibiting CdS photocorrosoion. A consistent Z-scheme reaction mechanism is proposed for the catalytic H₂/O₂ production by CdS/Pt-N-TiO₂ and CdS/Pt-N-F-TiO₂ heterojunctions, taking into account the photoinduced e⁻/h⁺ dynamics as well as the interfacial {CdS}/{Pt-N/F-TiO₂} chemistry.

1. Introduction

Since Fujishima and Honda [1] firstly reported the photoelectrolysis of water over TiO₂, solar driven H₂-production *via* photocatalytic water splitting by semiconductors has attracted extensive research attention [2–4]. Among semiconductor photocatalysts, TiO₂ is recognized as the most popular candidates due to its high chemical stability, nontoxicity and low cost. However, it is well known that TiO₂ has two major drawbacks: (1) its large bandgap (3.2 eV for anatase phase) practically prohibiting its photoactivation by visible solar light photons (λ > 360 nm) and (2) the recombination rate of photogenerated electrons and holes, leading to a low quantum yield i.e. typically 0.7% during 5.5 h [5]. The combination of TiO₂ with narrow band-gap semiconductors, such as CdS [6] and MoS₂ [7], forming a heterostructure has been proposed to extent the absorption of TiO₂ to the

visible light region [8]. To decrease the h⁺/e⁻ recombination rate, deposition of Pt° [9], Au° [10], and Ag° [11] nanoparticles on the TiO₂ surface is an efficient method to gather the photogenerated electrons, thus efficiently decreasing the recombination rate of charge carriers [12].

Recently, noble-metal doped TiO₂ photocatalysts such as Pt-TiO₂ [13] and Pd/Pt/Rh-TiO₂ [14] have been successfully used for H₂ production *via* photocatalytic water splitting. In the same direction, in order to extent the photocatalytic activity in the visible light region, Pt/N-TiO₂ co-doped photocatalysts have been successfully studied [15] for photocatalytic hydrogen production. Another approach to promote the photocatalytic hydrogen evolution is the design of ternary photocatalysts such as TiO₂-Au-CdS [8,16,17] or TiO₂-Pt-CdS [18–20]. Focusing on the preparation procedure, Park et al. [19] have shown that the configuration {CdS/Pt-TiO₂}(i.e. CdS-attached on preformed Pt-

---

Table 1

The compositions of sols employed for the preparation of all CdS/Pt-TiO$_2$, CdS/Pt-N-TiO$_2$ and CdS/Pt-N,F-TiO$_2$ prepared photocatalysts.

Code Name	H$_2$PtCl$_6$ (g)	NH$_4$Cl (g - mol)	NH$_4$F (g - mol)	TBOT (ml - mol)	Total %w.t. Pt content	total sol volume (ml)
0.5%Pt-TiO$_2$	0.004	–	–	3.4-0.01	0.5	50
0.5%Pt-N-TiO$_2$	0.004	0.53-0.01	–	3.4-0.01	0.5	50
0.5%Pt-N,F-TiO$_2$	0.004		0.37-0.01	3.4-0.01	0.5	50

Code Name	0.5%Pt-TiO$_2$ (g)	0.5%Pt-N-TiO$_2$ (g)	0.5%Pt-N,F-TiO$_2$ (g)	Na$_2$S	Cd(CH$_3$COO)$_2$	total volume
0.5%Pt-TiO$_2$CdS$_R$0.5 mM	1	–	–	0.078	0.572	100
0.5%Pt-TiO$_2$CdS$_R$1 mM	1	–	–	0.156	1.144	100
0.5%Pt-N-TiO$_2$CdS$_R$0.5 mM	–	1	–	0.078	0.572	100
0.5%Pt-N-TiO$_2$CdS$_R$1 mM	–	1	–	0.156	1.144	100
0.5%Pt-N,F-TiO$_2$CdS$_R$0.5 mM	–	–	1	0.078	0.572	100
0.5%Pt-N,F-TiO$_2$CdS$_R$1 mM	–	–	1	0.156	1.144	100

TiO$_2$ particles) has significantly higher photocatalytic activity than the {TiO$_2$/Pt-CdS} configuration (TiO$_2$-attached on preformed Pt-CdS particles). The high efficiency of {CdS/Pt-TiO$_2$} was suggested to result from a thermodynamically allowed vectorial electron transfer *via* the route CdS → TiO$_2$ → Pt [19]. In their more recent report, Park et al. [20] have shown that the crystal phase of CdS in CdS-Pt-TiO$_2$ plays a significant role for the photocatalytic H$_2$ evolution. More specifically, it has been found that cubic CdS (hereafter CdS$_R$) -obtained via dropping of aqueous Cd^{2+} in aqueous sulfide solution (i.e. Pt-TiO$_2$ suspension with equal molar ratios S^{2-}) has a > 10-fold higher hydrogen production i.e. 0.66 μmol H$_2$/min, than hexagonal CdS (0.077 μmol H$_2$/min)- obtained by simply reversing the dropping order (i.e., dropping S^{2-} to Pt-TiO$_2$ suspension with Cd^{2+}; hereafter Cd$_R$S).

In our recent report [21], Pt-loaded TiO$_2$, N-TiO$_2$ and N,F-TiO$_2$ photocatalysts were synthesized and evaluated for photocatalytic h$^+$/e$^-$ generation. An analysis of the correlation of Cr(VI) reduction and benzoic-acid oxidation with photodynamics of hole-electron (h$^+$-e$^-$) pair, monitored by EPR spectroscopy, revealed that, *lattice* Ti^{3+} in N,F-TiO$_2$ are deep electron trapping sites that are thermodynamically less efficient than *surface*-Ti^{3+} in TiO$_2$ and N-TiO$_2$ [21]. Accordingly, the reduction efficiency by the Ti^{3+}-surface electrons was enhanced in Pt-N-TiO$_2$ photocatalysts, while inhibited in Pt-N,F-TiO$_2$ [21].

So far, the use of N, F codoping on TiO$_2$ in combination with CdS for photocatalytic overall water splitting has not been exploited. Our hypothesis is that N, F incorporation in TiO$_2$ enables control/optimization of the h + /e- photodynamics *inside* the TiO$_2$ particles, while CdS allows control/optimization of the e-transfer events to H$_2$O substrate towards H$_2$/O$_2$ production. Accordingly, herein we take a step forward, to study the effect of CdS particles anchored on Pt-TiO$_2$, Pt-N-TiO$_2$ and Pt-N,F-TiO$_2$ photocatalysts and to evaluate the photoredox mechanism of obtained ternary photocatalysts in water splitting.

Specific goals of the present work are: [i] Preparation of CdS/Pt-TiO$_2$, CdS/Pt-N-TiO$_2$ and CdS/Pt-N,F-TiO$_2$ ternary hybrid photocatalysts. [ii] Evaluation of obtained ternary nanostructures for photocatalytic water splitting. [iii] Using EPR, to perform a quantitative monitoring of the photo induced hole/electron (h$^+$/e$^-$) dynamics, in conjunction with the measured H$_2$/O$_2$ production.[iv] Finally, the well-known problem of photo-corrosion of the CdS nanoparticles [22,23] was monitored quantitatively by measuring the leaching concentration of Cd^{2+} ions, by Anodic Stripping Voltammetry (ASV). We demonstrate that the N-doped TiO$_2$ material has a beneficial effect on CdS photocorrosion.

2. Experimental

2.1. Preparation of CdS$_R$/Pt-TiO$_2$, CdS$_R$/Pt-N-TiO$_2$ and CdS$_R$/Pt-N,F-TiO$_2$ photocatalysts

2.1.1. Preparation of 0.5%Pt-TiO$_2$, 0.5%Pt-N-TiO$_2$ and 0.5%Pt-N,F-TiO$_2$ precursors

The preparation of 0.5%Pt-TiO$_2$, 0.5%Pt-N-TiO$_2$ and 0.5%Pt-N,F-TiO$_2$ precursor catalysts was based on the sol – gel impregnation protocol developed in our previous work [21,31–33]. (i) 0.53 g NH$_4$Cl as N source and (ii) 0.37 g NH$_4$F as N,F source co-doping were diluted in 50 ml double distilled water, to obtain final [Ti:N] and [Ti:N,F] molar ratios equal to 1:1 and 1:1:1 respectively. In these solutions, 0.004 g, of H$_2$PtCl$_6$ was added to achieve the –optimum - final %wt. content of Pt to TiO$_2$ equal to 0.5% [20]. Then, 3.4 ml of Titanium butoxide (TBOT, Ti(OC$_4$H$_9$)$_4$, 97%) (equivalent to ≅ 1 g TiO$_2$ after hydrolysis) was added dropwise and the sol was stirred for 12 h, at RT = 24 °C, to achieve completion of the hydrolysis. The milky sol was spread on petri glass dishes and dried for 24 h at 120 °C under ambient atmosphere. The so obtained xerogels were calcined at 400 °C for 1 h with a 5 °C/min temperature ramp rate to obtain the final photocatalysts.

2.1.2. Preparation of CdS$_R$/Pt-TiO$_2$, CdS$_R$/Pt-N-TiO$_2$ and CdS$_R$/Pt-N,F-TiO$_2$ photocatalysts

Our preparation procedure was based on previous reports of Park *et al.* 2008 & 2011 [19,20]. More specifically, the CdS concentration was fixed to 1 mM or 0.5 mM. For the precipitation of CdS particles, aqueous Cd(CH$_3$COO)$_2$ was dropwise added in aqueous Na$_2$S (Table 1) solution to obtain the active Hawleyite CdS crystal phase [20]. Thus, for the preparation of CdS$_R$/Pt-TiO$_2$, CdS$_R$/Pt-N-TiO$_2$ and CdS$_R$/Pt-N,F-TiO$_2$ photocatalysts, 1 g of 0.5%Pt-TiO$_2$, 0.5%Pt-N-TiO$_2$ and 0.5%Pt-N,F-TiO$_2$ was suspended respectively in a 100 ml total volume aqueous Na$_2$S solution, where the equimolar amount of Cd^{2+} was dropped in a rate of 100 μl /min. The obtained catalysts were washed with distilled water 4 times and dried at 110 °C for 24 h under ambient atmosphere. Full details of the chemical conditions used for each sample, are listed in Table 1.

2.2. Characterization techniques

2.2.1. Powder X-ray diffraction

Powder X-ray diffraction (pXRD) patterns were obtained by the using of a Brüker Advance D8 system generating monochromated CuKa (λ = 1.5418 Å) radiation with continuous scanning rate of 2° min^{-1} in the range 10∘ < 2θ < 80∘ and operating voltage and current of 40 kV and 40 mA, respectively. The XRD patterns were assigned using the Joint Committee on Powder Diffraction Standards (JCPDS) database and then were analyzed with Rietveld refinement using an applicable computer program.

2.2.2. High resolution transmission electron microscopy (HR-TEM)

The nanostructure as well as materials phase composition was studied by a FEI CM20 HR20 h-TEM equipped with a Gatan GIF 200 Energy Filter.

2.2.3. X-ray photoelectron spectroscopy (XPS)

XPS measurements were performed under ultrahigh vacuum conditions with a base pressure of $2-5 \times 10^{-10}$ mbar in a SPECS GmbH instrument equipped with a monochromatic Mg Kα source ($h\nu = 1253.6$ eV) and a Phoibos-100 hemispherical analyzer. Samples were placed on silicon substrates and left in high vacuum before being placed in the main chamber for XPS measurement. The energy resolution was set to 1.18 eV, and the photoelectron take-off angle was 45° with respect to the surface normal. Recorded spectra were the average of three scans with the energy step set to 0.1-0.2 eV and a dwell time of 1 s. All binding energies were referenced to the C 1s core level at 284.5 eV. Spectral analysis included a Shirley background subtraction and peak deconvolution employing mixed Gaussian–Lorentzian functions in a least-squares curve-fitting program (WinSpec).

2.2.4. Electronic paramagnetic resonance (EPR)

Electronic Paramagnetic Resonance (EPR) spectra were recorded with a Brüker ER200D spectrometer equipped with an Agilent 5310 A frequency counter, operating at X- band (9.61 GHz). All the EPR experiments were running out under home-made software based on Lab View. *In situ* illumination of the samples inside the EPR cavity was performed using a 450 W Xe -light lamp (Oriel model 66929), equipped with a water IR cut-off filter.

2.2.5. Quantitative EPR monitoring of photogenerated h^+ and e^-

The study of the photo-generated holes and electrons in the nanoparticles, was realized by putting 50 mg of powder in a 3 mm quartz tube (Wilmad). For the quantification of surface and lattice electrons, 20 mg of catalyst were mixed with 100 μl isopropanol as h^+ scavenger in EPR tube and measured at 77 K. When necessary, various long pass filters were used: 325 nm (Oriel Corporation, 59460) and 400 nm (Edmund optics, 84754).

2.2.6. Estimation of the energy band-gaps

UV–vis-DRS spectra were recorded with a PerkinElmer (Lamda35) spectrophotometer equipped with integrating sphere assembly in the wavelength range of 300–800 nm. The band gap (E_g) values, were calculated using the Kübelka Münk Eq. (1a) [12]:

$$F_{R_\infty} = \frac{(1 - R_\infty)}{2R_\infty} = \frac{k}{s} \tag{1a}$$

F_{R_∞} is the so-called Kübelka–Münk function, k and s are K–M absorption and scattering coefficients, respectively.

From Eq. (1a) we can easy derive Eq. (1b) [12]:

$$ah\nu = C_1(h\nu - E_g)^{1/2} \tag{1b}$$

where $h\nu$ is the phonon energy, C_1 is proportionality constant.

Fourier Transform –Infrared transparence spectra (FT-IR) were recorded using a Nicolet IS$_5$ system equipped with an OMNIC software package in the range of 4000-400 cm^{-1} (Fig. S1).

Thermogravimetric Analysis (TGA) of catalysts were carried out by heating rate of 10 °C/min up to 800 °C and using a Shimadzu DTG -60 analyzer, while the analysis of thermogravimetric data was realized by the TA-60WS application (Fig. S3).

Monitoring Photocorrosion of CdS via Cd^{2+} leaching: The leaching of Cd^{2+} from degraded CdS was determined by an Anodic Stripping Voltammetry (ASV) Trace Master5-MD150 polarograph by Radiometer Analytica. A hanging mercury drop electrode (HMDE) was used as the working electrode, with Hg^{2+} drop 0.4 mm diameter, generated at the edge of a 70 μm capillary. The reference electrode was Ag/AgCl, and the counter electrode was Pt°. Before the stripping step, N$_2$ gas

(99.999% purity) was passed from the measuring solutions to remove any O$_2$ traces, while the solution was kept under continuous stirring. The ASV signal intensities were calibrated by using a Cd(NO$_3$)$_2$ standard solution. This set up allows for a very accurate detection of Cd^{2+} at the level of 1 ppb [24,25]. For a typical photoleaching Cd^{2+} measuring experiment, the concentration of the photocatalyst was 178 mg /L, under Ar atmosphere and vigorous stirring. The source of irradiation was a mercury lamp (125 W), equipped with an IR cut –off filter. At specific time intervals (t = 0, 1 h, 2 h and 3 h) during photocatalytic process, 10 ml of sample was withdrawn for ASV analysis.

2.3. Photocatalytic water splitting

The photocatalytic water splitting reactions were carried out in an immersion-well reactor (Photochemical Reactors Ltd., UK) composed of a medium-pressure mercury lamp (Model 3010,125 W, discharge length 30 mm, light output 7×10^{18} photons /sec). The double-walled immersion reactor was made of quartz glass (Model 3210) and a standard reaction flask provided with two angle sockets and one vertical socket of total reaction volume of 300 ml. In each photocatalytic reaction, 50 mg of the catalyst were suspended into 275 ml distilled water (final concentration 0.18 g/L), while the temperature was adjusted at 34 ± 3°C, via continuous cooling tap-water system. Before the beginning of each experiment, a vacuum pump (model: KNF N035.AT.18, 10^{-4}bar pressure) was used to remove any gas trace from the reaction medium. Afterwards, the suspension was continuously bubbled with Ar gas (99.997%). Quantitative monitoring of produced H$_2$/O$_2$ was realized using a continuous online Gas Chromatography System combined with a Thermo-conductive Detector (GC-TCD- Shimadzu GC-2014, carboxen 1000 column, Ar carrier gas).

3. Results

3.1. pXRD analysis

In Fig. 1 pXRD plots for all CdS$_R$/Pt-TiO$_2$, CdS$_R$/Pt-N-TiO$_2$ and CdS$_R$/Pt-N,F-TiO$_2$ photocatalysts are presented. Rietveld analysis [26] of the obtained XRD data was performed, (Table 2) setting as adjustable parameters the % of each crystal phase, cell parameters (a, b, c), cell volume, crystal size and the reliability factors E% (profile factor) and R % (weighted profile factor). The cell parameters in Table 2 for all prepared solids show a small difference *vs.* the theoretical values of pure TiO$_2$ anatase phase and pure CdS Hawleyite phase. Such –small-differences are indicative of the incorporation of dopants in the crystal structure in accordance with literature [19,20,26].

By a perusal of Fig. 1 and Table 2 it is discerned that:

[i] *Regarding the phase composition*: photocatalytic active TiO$_2$ anatase crystal phase (CSD9854) is obtained for all photocatalysts. Importantly, the more- photoactive cubic CdS Hawleyite sphalerite [20], than less-photoactive hexagonal CdS greenockite [20], crystal phase is obtained for all photocatalysts.

[ii] *On the stoichiometry and mass-balance*: small amounts i.e. < 0.5% of Pt NPs were formed in all photocatalysts. The CdS Hawleyite sphalerite percentage accounts well for the initial Cd^{+2} and S^{-2} concentrations used i.e. indicating that the added Cd^{+2} and S^{-2} were almost stoichiometrically incorporated into the solid phases (Table 2).

[iii] *Regarding the particle sizes*: small anatase crystals size varying from 7 to 10 nm are obtained for all prepared photocatalysts. Small cubic CdS Hawleyite sphalerite crystals d˜2.0–2.3 nm is obtained for all prepared photocatalysts. As we show hereafter, these fine cubic CdS particles on the TiO$_2$ anatase are of key- beneficial importance for the photocatalytic activity of these photocatalysts.

3.2. HRTEM

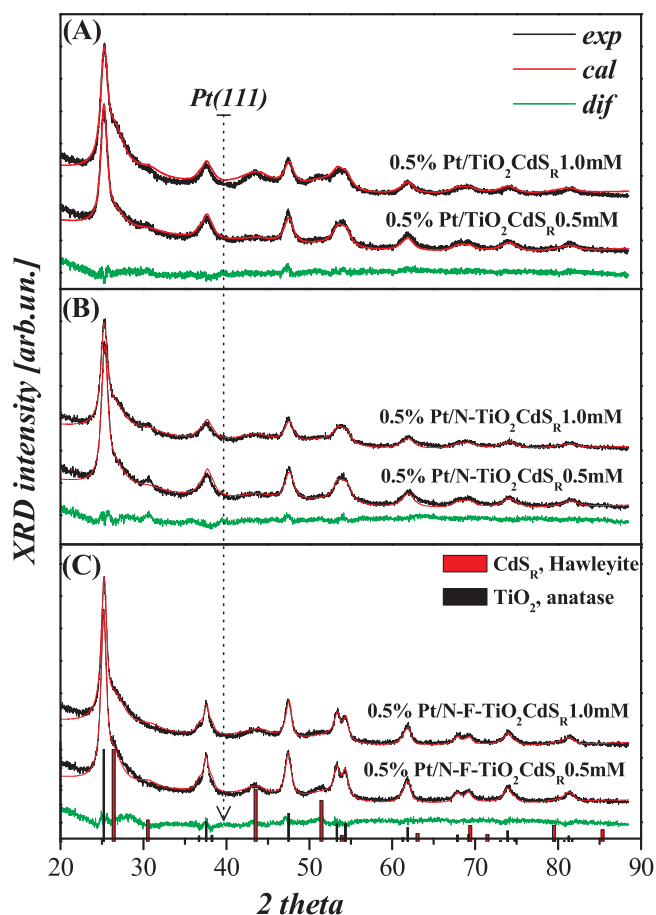In Fig. 2, a High Resolution Transmission Electron Microscopy

Fig. 1. pXRD data for **(A)** Pt/ TiO$_2$CdS$_R$, **(B)** Pt/N-TiO$_2$CdS$_R$ and **(C)** Pt/N-F-TiO$_2$CdS$_R$ hybrid photocatalysts. The anatase and CdS$_R$ Hallowsite crystal phase are marked by the column bars at the bottom of plots. Dotted lines denote the Pt (1 1 1) reflection.

(HRTEM) image of [0.5% Pt/N-TiO$_2$CdS$_R$0.5 mM] material is presented. In the left-panel, lattice fringes with a spacing of d = 0.352 nm corresponding to (101) TiO$_2$ planes can be resolved. In addition, orthogonal lattice fringes with spacings d = 0.359 nm, marked as A in the inset, and with d = 0.336 nm, marked as B in the inset, corresponding to (100) and (002) CdS planes respectively can be resolved. Small Pt particles are dispersed on the CdS-TiO$_2$ heterostuctures, are evidenced in the TEM images. Thus the HRTEM data, are in accordance with the XRD data, and show that the Pt/N-TiO$_2$CdS$_R$ material –which as we show hereafter has the best photocatalytic performance- is a ternary Z-heterostructure with CdS-particles finely dispersed on the TiO$_2$ matrix.

3.3. DRS measurements

In Fig. 3a, the Diffuse Reflectance of UV–vis spectra for the materials are presented. As we can observe, the CdS-containing photocatalysts have 2 characteristic bands i.e. in UV (330–345 nm) & visible region (470–498 nm). The visible absorption is contributed to d-d transition of CdS catalyst [22,27], linked to interfacial charge transfer absorption from the Conduction Band (CB) of TiO$_2$ to the Valence Band (VB) of CdS [28]. Close inspection, shows that Pt contributes to creation of a distinct shoulder at 560 nm. As we have shown in our previous work [21] the light absorption of 560 nm is attributed to Pt^{2+} → Pt^{4+} intervalence charge transfer [21,29].

Pt-TiO$_2$-N/CdS$_R$, and Pt-TiO$_2$-N-F/CdS$_R$, catalysts have a more extended absorption towards visible wave-lengths, because of the insertion of Nitrogen in the crystal lattice of TiO$_2$. Notice that, absorption of visible photons is higher for Pt-TiO$_2$-N-F/CdS$_R$ than Pt-TiO$_2$-N/CdS$_R$.

This is because F anions help the N anions to penetrate deeper into the TiO$_2$ anatase lattice, creating defects [30–32]. Also, the samples with higher concentration of CdS have a quite higher absorbance intensity, with a blue shift of band edge from 544 nm to 588 nm [22,27].

The band gaps, E$_g$, of all hybrid photocatalysts were calculated from Kübelka- Münk plots [12], and are listed in Table 4. From the Eg values we can conclude that: **(a)** all the CdS-containing TiO$_2$ photocatalysts have two band gaps where the values range from E$_{g1}$ = 3.17 to 2.81 eV (attributed to TiO$_2$) and E$_{g2}$ = 2.08 to 2.19 eV (attributed to CdS), **(b)** the narrower band gaps of Pt/TiO$_2$, combined with CdS is because of the interaction of conduction band of TiO$_2$ with the valence band of CdS, facilitating the separation and transfer of photo-induced charge carriers in the hybrid structure, **(c)** the narrower band gaps of Pt-TiO$_2$/N-CdS$_R$ and Pt-TiO$_2$/N-F-CdS$_R$ are because of the insertion of N-atoms in the TiO$_2$ lattice, **(d)** the lower E$_g$ value in the case of N/F doped samples, is because of the contribution of the Fluoride anion to the incorporation of Nitrogen anion deeper to the lattice, creating more Oxygen Vacancies (OVs). **(e)** modification of the samples with Pt have no influence to the band gap of all hybrid photocatalysts.

3.4. XPS analysis

XPs data for the [0.5% Pt/N-TiO$_2$CdS$_R$0.5 mM] material are presented in Fig. S4 of Supplementary Information. In the Ti 2p spectrum, Ti^{4+} in TiO$_2$ is evidenced by the doublet Ti 2p$_{3/2}$ (binding energy 458.5 eV) and Ti 2p$_{1/2}$ (binding energy 464.4 eV [33]. The signal at binding energy 457.3 eV is consistent with Ti^{3+} [33], centers detected also be EPR hereafter. The Cd$_{3d}$ region peaks at 404.7 eV and 411.5 eV, are assigned to the binding energies of Cd 3d$_{5/2}$ and Cd3 d$_{3/2}$, suggesting the existence of Cd^{2+} in hexagonal CdS, while at 406.5 eV and 413.3 eV region is duo to Cd^{2+} in cubic phase with states Cd 3d$_{5/2}$ and Cd 3d$_{3/2}$ [34,35]. O1 s spectrum of TiO$_2$ has three fitted peaks at 529.9 eV, 530.3 eV and 533.0 eV correspondingly. The first and second one are attributed to the lattice oxygen of TiO$_2$ [36] while the 533.0 eV peak could be assigned to OH [36,37]. Finally, the S$_{2p}$ spectrum, consistent with 2 characteristic peaks of binding energy 161.3 eV and 162.4 eV is characteristic for CdS nanoparticles [38].

3.5. EPR study of the holes-electrons' photodynamics in CdS$_R$/Pt-TiO$_2$, CdS$_R$/Pt-N-TiO$_2$ and CdS$_R$/Pt-N,F-TiO$_2$ photocatalysts

In Fig. 4(A) the EPR spectra were recorded under UV–vis light full irradiation (λ > 190-1100 nm), while in Fig. 4(B) & (C) UV (λ < 340 nm) and visible light (λ > 400 nm) irradiation, was recorded. All spectra correspond to [light] minus [dark] EPR signals, thus they represent exclusively photoactive centers.

According to previous reports by our group [21,31,32,39] and others [40–42] in a typical anatase-TiO$_2$ EPR spectrum (Fig. 4(A)) the main detected photoinduced signals are due to:

[i] *photoinduced holes (h$^+$):* these can be of two-types [40,41] (see Table 3) (a) 'external' [Ti(IV)-O-Ti(IV)-O˙] holes with the O˙ localized on the surface of the nanoparticle, recognized by their rhombic g-tensor g = [2.025, 2.014, 2.003]; (b) 'internal' [Ti(IV)-O˙-Ti(IV)-OH] holes with the O˙ localized in the lattice of the nanoparticle characterized by a more axial g-tensor g = [2.018, 2.014, 2.003].

[ii] *photoinduced electrons (e$^-$):* these correspond to Ti(III) states located either inside the lattice or on the surface of the nanoparticle [31,41,42] (see Table 3). Lattice electrons are characterized by sharp Ti(III) EPR signals, due to well defined local environment in the TiO$_2$ lattice [21,31,40,42], with g = 1.989. Surface Ti(III) are characterized by broad EPR signals, due to the electron delocalization on the low-symmetry surface of the TiO$_2$ particle [40].

3.5.1. Photodynamics of h$^+$/e$^-$ in CdS$_R$/Pt-TiO$_2$

3.5.1.1. UV–vis irradiation. In Fig. 4(A) under UV–vis irradiation, the photogeneration of internal [Ti(IV)- O˙-Ti(IV)-OH] holes, easily

Table 2
Results of PXRD with Rietveld analysis values of all CdS/Pt-TiO$_2$, CdS/ Pt-N-TiO$_2$ and CdS/Pt-N,F-TiO$_2$ prepared photocatalysts.

| code name	Crystal phase	space group	%	a	b	c	d(nm)	cell volume (A^3)	E%	R%
TiO$_2$ CSD9854	anatase	Tetragonal I41	–	3.797	3.797	9.579	–	138.1	–	–
CdS CSD31075	Hawleyite sphlerite	F-43m	–	5.820	5.820	5.820	–	197.1	–	–
Pt CSD41525	Platinum	Fm-3m	–	3.970	3.970	3.970	–	62.6	–	–
0.5%Pt-TiO$_2$	Anatase	Tetragonal I41	89.9	3.786	3.786	9.474	**9.7**	143.93	12.8	15.3
	Brookite-	Orthrombic Pcba	8.9	9.135		5.472	**6.2**	274.90		
	Pt	CubicFm-3m	0.2	3.999	3.999	3.999	**n.d.**	63.9		
0.5%Pt-TiO$_2$CdS$_R$0.5 mM	Anatase	Tetragonal I41	88.3	3.856	3.856	9.658	**7.9**	143.6	12.9	17.8
	CdS Hawleyite	Cubic: F-43m	11.5	5.910	5.910	5.910	**2.3**	206.4		
	Pt	CubicFm-3m	0.2	3.999	3.999	3.999	**n.d.**	63.89		
0.5%Pt-TiO$_2$CdS$_R$1.0 mM	Anatase	Tetragonal I41	67.7	3.850	3.850	9.656	**7.8**	143.2	10.1	14.9
	CdS Hawleyite	Cubic: F-43m	32.1	5.924	5.924	5.924	**2.4**	207.9		
	Pt	CubicFm-3m	0.2	4.002	4.002	4.002	**n.d.**	64.09		
0.5%Pt-N-TiO$_2$	Anatase	Tetragonal I41	90.3	3.853	3.853	9.646	**10.4**	143.9	12.2	15.6
	Brookite-	Orthrombic Pcba	9.5	9.476	5.523	5.213	**7.1**	275.4		
	Pt	Cubic: Fm-3m	0.2	3.995	3.995	3.995	**n.d.**	64.34		
0.5%Pt-N-TiO$_2$ CdS$_R$0.5 mM	Anatase	Tetragonal I41	86.1	3.850	3.850	9.648	**7.9**	143.0	11.6	17.7
	CdS Hawleyite	Cubic: F-43m	13.7	5.894	5.894	5.894	**2.3**	204.8		
	Pt	Cubic: Fm-3m	0.2	3.995	3.995	3.995	**n.d.**	64.34		
0.5%Pt-N-TiO$_2$ CdS$_R$01.0 mM	Anatase	Tetragonal I41	81.1	3.853	3.853	9.657	**8.2**	143.3	12.9	17.3
	CdS Hawleyite	Cubic: F-43m	18.7	5.935	5.935	5.935	**2.3**	209.1		
	Pt	Cubic: Fm-3m	0.2	3.955	3.955	3.955	**n.d.**	63.99		
0.5%Pt-N,F-TiO$_2$	Anatase	Tetragonal I41	99.9	3.848	3.848	9.641	**8.8**	142.81	12.3	17.3
	Pt	Cubic: Fm-3m	0.1	4.006	4.006	4.006		64.27		
0.5%Pt-N-F-TiO$_2$ CdS$_R$0.5 mM	Anatase	Tetragonal I41	86.8	3.856	3.856	9.673	**10.3**	143.8	10.8	15.9
	CdS Hawleyite	Cubic: F-43m	13.0	5.933	5.933	5.933	**30**	208.9		
	Pt	Cubic: Fm-3m	0.2	3.986	3.986	3.986	**n.d.**	63.67		
0.5%Pt-N-F-TiO$_2$ CdS$_R$01.0 mM	Anatase	Tetragonal I41	75.4	3.856	3.856	9.667	**10.8**	143.74	11.4	14.8
	CdS Hawleyite	Cubic: F-43m	24.4	5.900	5.900	5.900	**2.3**	205.36		
	Pt	Cubic: Fm-3m	0.2	3.998	3.998	3.998	**n.d.**	63.92		

Bold fonts indicate the g-components detected in the present work.

discerned by their feature at g = 2.018, which is detected for both CdS$_R$0.5/Pt-TiO$_2$ and Pt- CdS$_R$1.0/TiO$_2$. In contrast, these internal holes are not detected in the reference Pt-TiO$_2$ i.e. only external [Ti(IV)-O-Ti (IV)-O˙] holes are appeared in Pt-TiO$_2$. Thus the presence of CdS quenches the external [Ti(IV)-O-Ti(IV)-O˙] holes, in accordance with the lower oxidation capacity reported recently for CdS$_R$-TiO$_2$ [20]. On the other hand, only a small Ti$^{(III)}$/e$^-$ signal is recorded, in either CdS$_R$0.5/Pt-TiO$_2$ or Pt- CdS$_R$1.0/TiO$_2$ hybrids and i.e. due to the capturing of the photogenerated electrons by the Pt nanoparticles [21].
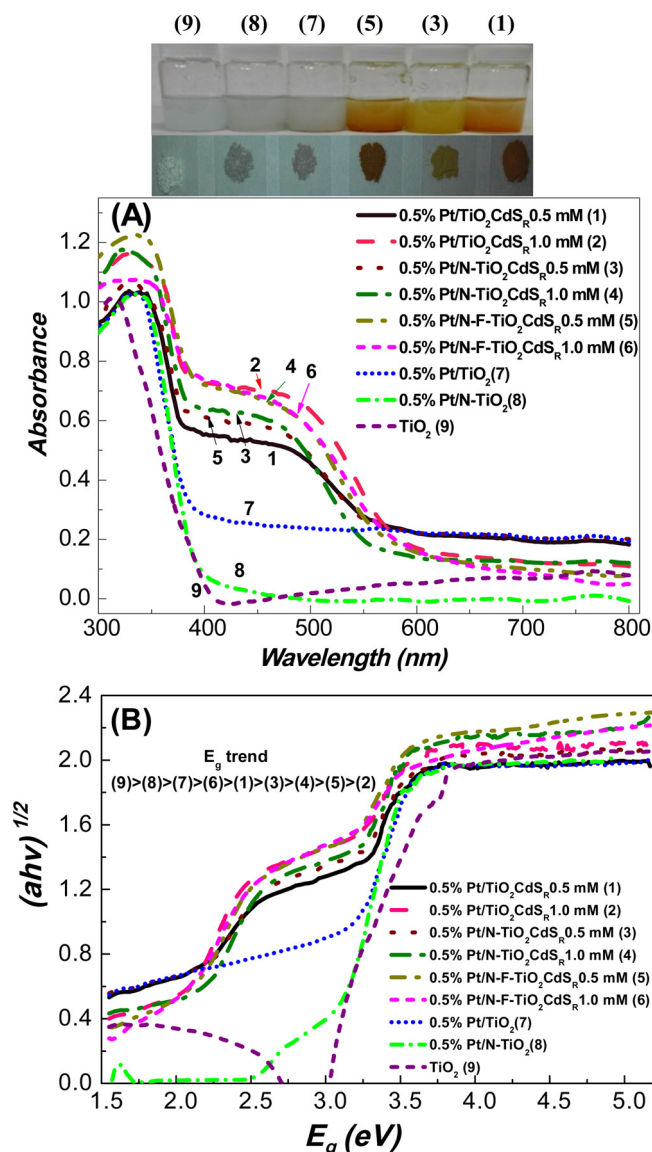
3.5.1.2. Selective   UV-irradiation   λ < 325 nm   or   vis-irradiation,

λ > 400 nm. Comparison of the EPR data with selective irradiation under UV-light λ < 325 nm (Fig. 4(B)) vs. UV–vis light (Fig. 4(A)) shows that the types of photogenerated species are identical. The signal intensities under UV < 340 nm are ˜85% of the signal intensities under UV–vis light, indicating that the photocatalysts are primarily –but not exclusively- activated by UV-photons. Indeed, when we compare the EPR spectra under Visible photons, λ > 400 nm, (Fig. 4(C)), these account for ˜15% of the signal intensities, in comparison with UV i.e. Fig. 4(B) *vs.* (C).

To better understand the role of CdS, the h$^+$/e$^-$ photodynamics of CdS$_R$/TiO$_2$, was studied. The EPR data (see trace 4 in Fig. 4(B) (UV
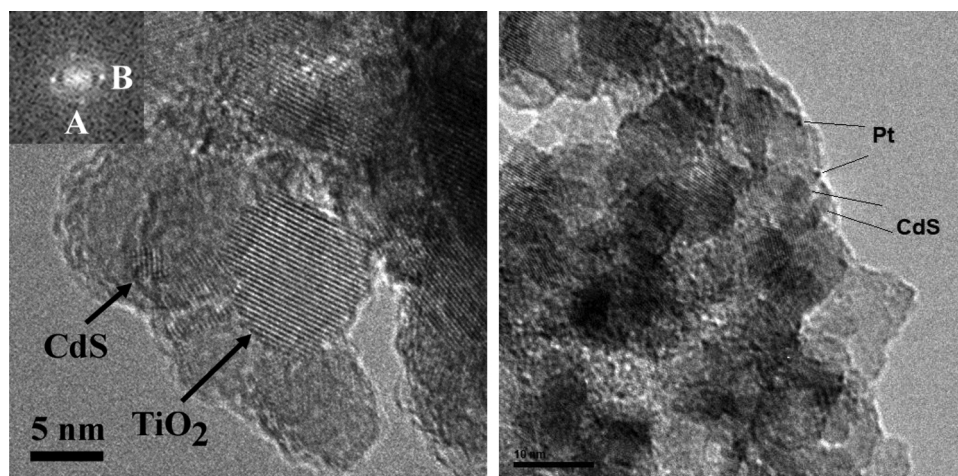
Fig. 2. HRTEM images for Pt/N-TiO$_2$CdS$_R$ material. In the left-panel the (101) TiO$_2$ lattice fringes and (100), (002) CdS lattice fringes. The inset shows local fast Fourier transform of the CdS nanoparticle with spot A corresponding to a lattice spacing of d = 0.359 nm and spot B to d = 0.336 nm.

Fig. 3. (A) DRS –UV-Vis spectra & **(B)** Kübelka –Münk plot for all Pt/TiO$_2$CdS$_R$, Pt/N-TiO$_2$CdS$_R$, Pt/N-F-TiO$_2$CdS$_R$ hybrid photocatalysts. ***Inset photo:*** dispersion solution & powder of the samples.

signals under UV < 340 nm. This indicates that, in CdS$_R$/TiO$_2$, the electrons' migration mechanism from the conduction band of CdS to conduction band of TiO$_2$ is –partially- active under visible light irradiation. This is in accordance with the DRS-UV–vis spectra which show that CdS$_R$ can adsorb photons both in UV and in the visible light region.

3.5.1.3. Photodynamics of $h^+/e-$ in CdS_R/Pt-N-TiO$_2$ hybrids. the photoinduced EPR spectra of N-doped CdS$_R$0.5/Pt-N-TiO$_2$, CdS$_R$1.0/Pt-N-TiO$_2$ and Pt-N-TiO$_2$ and CdS$_R$/N-TiO$_2$ are presented in Fig. 5. In all N-doped materials the same g-tensors of photogenerated holes (2.025, 2,018, 2,014) and photogenerated Ti$^{(III)}$ electrons are observed as in the case of Pt-TiO$_2$ samples i.e. denoted with dotted lines. As observed in Figs. 4 and 5 there are two main differences between the spectra of {Pt-N-doped} *vs.* {Pt-TiO$_2$}samples:[i] In the right part of the EPR spectrum for Pt-N-TiO$_2$, stronger photogenerated Ti(III)/e- signals are recorded in comparison to Pt-TiO$_2$. As we have demonstrated recently [21,31] this higher amount of photogenerated electrons is attributed to the supporting electron production mechanism by the N$_b$ sites

$$N_b- \rightarrow N_b^{\cdot} + e- \tag{1}$$

in N-doped samples [19,31,43].

[ii] in the left part of the EPR spectrum for CdS$_R$0.5/Pt-N-TiO$_2$, CdS$_R$1.0/Pt-N-TiO$_2$ and Pt-N-TiO$_2$ an extra photo-induced signal with a feature at g = 2.009 is detected, corresponding to the g$_{yy}$ component of O$_2$$^{\cdot-}$ superoxide species stabilized on the surface of Ti^{4+} anatase ions [44], by the photoexcited electrons, according to the mechanism:

$$N_b^- + O_{2(gas)} \rightarrow N_b^{\cdot} + O_2^{\cdot-}{}_{(surf)} \tag{3a}$$

$$N_b^{\cdot} + O_{2(gas)} \rightarrow N_b^+ + O_2^{\cdot-}{}_{(surf)} \tag{3b}$$

As discussed in detail previously [21,31,32,39] the detection of such photoexcited O$_2$$^{\cdot-}$ species is a direct proof of the enhanced reduction ability of N-doped TiO$_2$. Under visible-light irradiation (> 400 nm) Fig. 5(C) a significant increase of O$_2$$^{\cdot}$- signal (g = 2.009) is recorded. This signal is a direct evidence that the mechanism described by reaction (3a), (3b) takes place mainly in the visible-light region at N-doped TiO$_2$ as shown previously [44,45]. Finally, we underline that the photogeneration of O$_2$$^{\cdot-}$ is always higher in CdS$_R$0.5/Pt-N-TiO$_2$ *vs.* CdS$_R$1.0/Pt-N-TiO$_2$, for both under UV or visible light irradiation. This implies that the O$_2$$^{\cdot}$- photoinduced mechanism is faster in CdS$_R$0.5/Pt-N-TiO$_2$ than in CdS$_R$1.0/Pt-N-TiO$_2$.

To distinguish the role of Pt *vs.* CdS$_R$ we note that enhanced Ti$^{(III)}$/e$^-$ photogeneration is observed in the non-platinized CdS$_R$/N-TiO$_2$ material (trace 4 in Fig. 5) under either UV or visible light irradiation. Thus, the e$^-$ migration mechanism from CdS conduction band to N-TiO$_2$ conduction band is also active in the non-platinized CdS$_R$/N-TiO$_2$ as in the platinized CdS/Pt-N-TiO$_2$.

3.5.1.4. Photodynamics of h^+/e^- in CdS/Pt-N,F-TiO$_2$ hybrids. In Fig. 6(I) & Fig. 6(II) the h$^+$/e$^-$ photodynamics of CdS$_R$0.5/Pt-N,F-TiO$_2$, CdS$_R$1.0/Pt-N,F-TiO$_2$ are investigated. In comparison with TiO$_2$ and N-TiO$_2$ samples discussed above, the N-F co-doped TiO$_2$ is characterized by sharp EPR signals of *lattice* Ti$^{(III)}$ ions with g~ 1.989 in the right part of the EPR spectra. As shown previously [21,31,43,45]

irradiation)) shows an enhancement of all surface Ti$^{(III)}$/e$^-$ signals (g values 1.972, 1.954, 1.93, marked by the hatched part in Fig. 4(B)). This enhancement of surface Ti$^{(III)}$/e$^-$ is indicative of electron migration from CdS$_R$ conduction band to TiO$_2$ conduction band, which is known to take place in coupled CdS/TiO$_2$ composites photocatalyst [6–8,19,20].

Under visible light irradiation (λ > 400 nm, trace 4 in Fig. 4(C)) the Ti$^{(III)}$/e$^-$ EPR signals of CdS$_R$/TiO$_2$ are ~20% vs. the Ti$^{(III)}$/e$^-$ EPR

Table 3

g- and ^{14}N (I = 1) hyperfine-tensors of observed paramagnetic species in all all CdS/ Pt-TiO$_2$, CdS/ Pt-N-TiO$_2$ and CdS/Pt-N,F-TiO$_2$ prepared catalysts.

Paramagnetic species	g$_1$	g$_2$	g$_3$	A$_1$/Gauss	A$_2$/Gauss	A$_3$/Gauss	g$_1$	g$_2$	g$_3$
N$_b$$^{\cdot}$	2.005	2.004	2.003	2.3	4.4	32.3			
O$_2$$^{\cdot-}$	2.025	**2.009**	2.003						
Ti^{+3} lattice							**1.989**	1.964	1.94
Ti^{+3} surface							**1.972**	1.954	**1.93**
Ti(IV)-O-Ti(IV)-O$^{\cdot}$	**2.025**	**2.014**	2.003						
Ti(IV)-O$^{\cdot}$-Ti(IV)-OH	**2.018**	**2.014**	2.003						

Bold fonts indicate the g-components detected in the present work.

Table 4

Rate gas evolution of H2 and O2 production, in comparison with photo generated trapped holes h+ ($I_{Ti^{4+}-O\cdot^- Ti^{4+}-OH^-}$), surface electrons e- ($I_{Tisurface}^{3+}$) and lattice electrons ($I_{Tilattice}^{3+}$), detected by EPR.

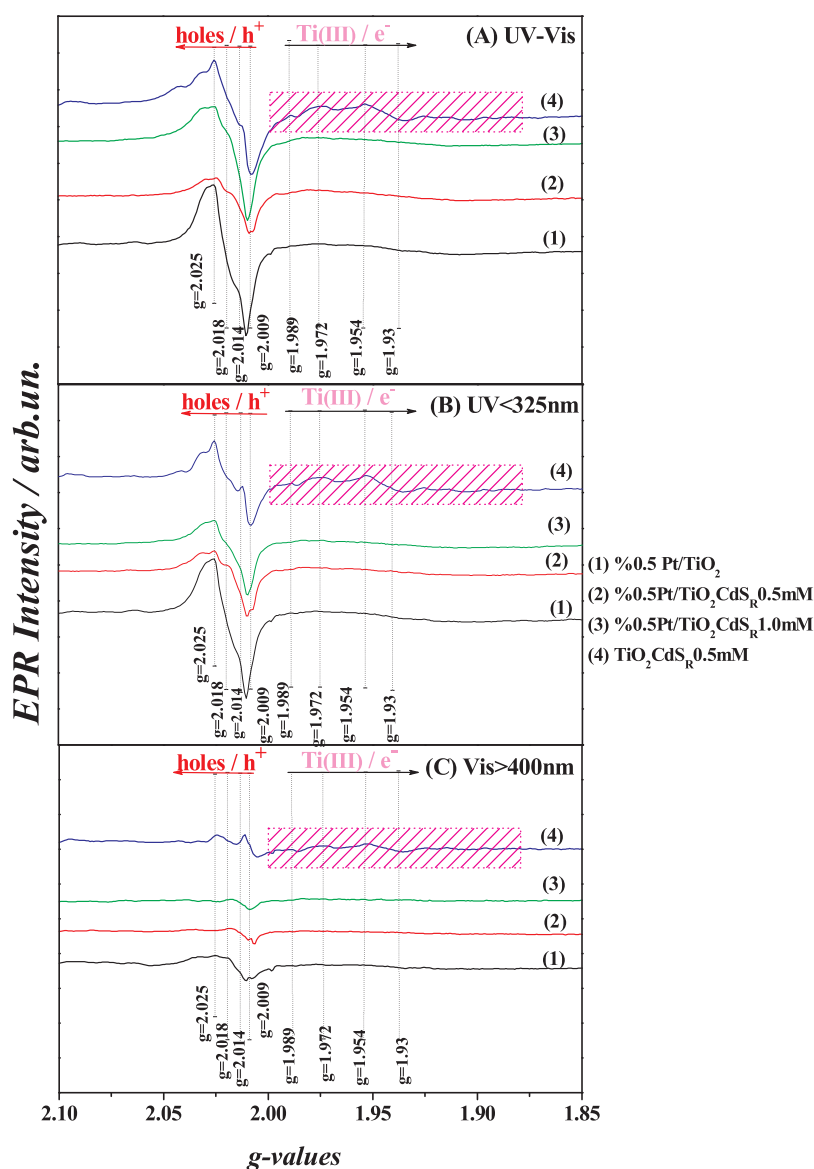| Code Name	Rate (μmol/g/h)		Eg (eV)		$I_{Ti^{4+}-O\cdot^- Ti^{4+}-OH^-}$ (h+) (g = 2.025) (x10^{-4})	$I_{Tilattice}^{3+}$ (e$^-$) (g = 1.989) (x10^{-4})	$I_{Tisurface}^{3+}$ (e$^-$) (g = 1.972) (x10^{-4})
	H2	O2	Eg1	Eg2			
0.5%Pt-TiO2CdSR0.5 mM	559.8	219.6	3.17	2.19	23	20	74
0.5%Pt-TiO2CdSR1.0mM	319.4	129.5	2.94	2.09	18	7	35
0.5%Pt-N-TiO2CdSR0.5 mM	639.2	319.8	3.02	2.21	45	29	79
0.5%Pt-N-TiO2CdSR1.0mM	398.8	179.8	2.90	2.20	5	21	50
0.5%Pt-N,F-TiO2CdSR0.5 mM	79.7	38.8	2.70	2.19	16	682	0
0.5%Pt-N,F-TiO2CdSR1.0mM	17.7	9.6	2.60	2.08	6	370	0
0.5%Pt-TiO2	–	–	3.20	–	7	8	37

higher *lattice*-Ti(III) photogeneration is the main difference between N/F co-doped and N-doped TiO2 samples. Lattice Ti(III) photogneration is enhanced by F ions which facilitate the incorporation of N ions deeper in the TiO2 lattice, thus creating more *lattice*-Ti(III) than *surface*-Ti(III).

With regard to the N$^-$ and O2$^-$ species, see left part of EPR spectra, a combination of the EPR signals of three paramagnetic species is detected, as follows:

[a] Nb· species with the signal triplet at g = 2.024, 2.004, 1.984 according to [32],

[b] O2–· species with the three characteristic peaks at g1 = 2.011, g2 = 2.001 and g3 = 1.974 [30] and [c] {Ti^{4+}-O$^-$-Ti^{4+}-OH$^-$} hole species with the g component at 2.016 are photogenerated in anatase

Fig. 4. EPR spectra (light minus dark) for of Pt/TiO2CdSR, at 77 K. All signals were recorded under: (**A**) UV–vis (**B**) UV λ < 325 nm (**C**) Visible λ > 400 nm, light irradiation.
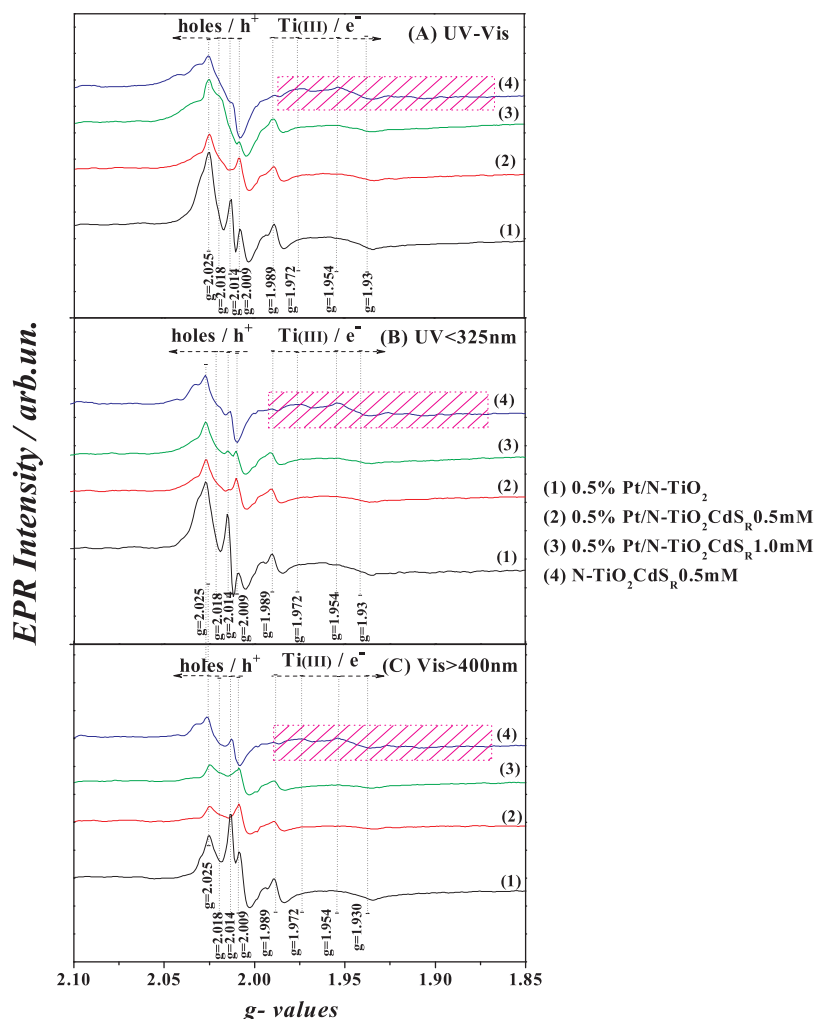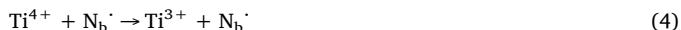
Fig. 5. EPR spectra (light minus dark) for of Pt/N-TiO₂CdS$_R$, at 77 K. All signals were recorded under (**A**) UV–vis (**B**) UV λ < 325 nm (**C**) Visible λ > 400 nm, light irradiation.

[41].

Mechanism-wise, lattice Ti$^{(III)}$ and N$_b$˙ species support the visible-light induced photoredox mechanism (4) [21,31,43,45]:

$$Ti^{4+} + N_b˙ \rightarrow Ti^{3+} + N_b˙ \tag{4}$$

Comparing the EPR signals of CdS0.5/Pt-N,F-TiO₂, CdS1.0/Pt-N,F-TiO₂ samples is observed that in the right part of the spectra in Fig. 5, the lattice Ti$^{(III)}$ signals are consistently higher for CdS$_R$0.5/Pt-N,F-TiO₂. Also, this material produced lower amounts of N$_b$˙ species and higher amounts of O₂–˙ species, indicating that reactions (3a) and (3b) are more efficient in CdS$_R$0.5/Pt-N,F-TiO₂. The absence of surface e⁻ is contributed to the capacity of F-anion to act as an electron scavenger as it was previously described in our previous work [21] (see Fig. S2 with the using of isopropanol as hole scavenger and for quantification of e⁻ in Table 4).

Overall, from the analysis of the EPR signals for Ti$^{(III)}$ lattice N$_b$˙ & O₂–˙ species, it is concluded that 0.5 mM CdS$_R$ is the optimum loading N-doped as well as N/F-dopped materials.

When we compare to role of Pt vs. CdS$_R$, in Fig. 6 under UV–vis (see Fig. 6(**A**)), UV (see Fig. 6(**B**) < 340 nm) and Visible (see Fig. 6(**C**), λ > 400 nm), we conclude that:

In Pt-N,F-TiO₂ lattice Ti$^{(III)}$ ions, N$_b$˙ and O₂–˙ species are preferably photogenerated, while in CdS$_R$/N,F-TiO₂ or CdS$_R$/N-TiO₂ and CdS$_R$/TiO₂ a preferable enhancement of surface Ti$^{(III)}$/e- signal is recorded (see region denoted with dotted rectangular in Fig. 6). This reveals that

the e⁻ migration mechanism from conduction band of CdS$_R$ to the conduction band of {N,F-TiO₂}is active. Notice that in the left part of the CdS$_R$/N,F-TiO₂ EPR signal, a deactivation of photoexcited N$_b$˙ and O₂–˙ is evidenced, probably caused by the blocking of lattice Ti$^{(III)}$/e⁻ by the surface-migrating Ti$^{(III)}$/e⁻.

Overall, the EPR data provided a detailed picture of the photo-induced species and their –complex- interrelation. The electron shut-tling capacity of the CdS$_R$ is among the main mechanistic findings, as well as the observation that UV *and* visible light photons are involved in the photogeneration of the various species. All this knowledge is of pertinence to the photocatalytic water splitting efficiency of the materials, as we analyze in the following.

3.6. Photocatalytic water splitting towards H₂/O₂

The photocatalytic water splitting efficiency of the catalysts is illustrated in Fig S6(**A**) & Fig S6(**B**), while the rate of produced gases is presented in graph (Fig. 7). The GC-TCD analysis showed that in all cases, H₂ and O₂ were the only gas products from all studied catalysts with a molar ratio [H₂:O₂] = 1.9 ± 0.2 (Fig. S5). This [H₂:O₂] ratio ∼2 is an indication that the H₂ and O₂ gases are produced by H₂O splitting [46].

The undoped TiO₂, Pt/N-TiO₂ and Pt/N-F-TiO₂, and blank tests (no catalyst, dark), did not show any gas production, confirming that the water splitting is clearly a photo*catalytic* i.e. not a photolytic, process.

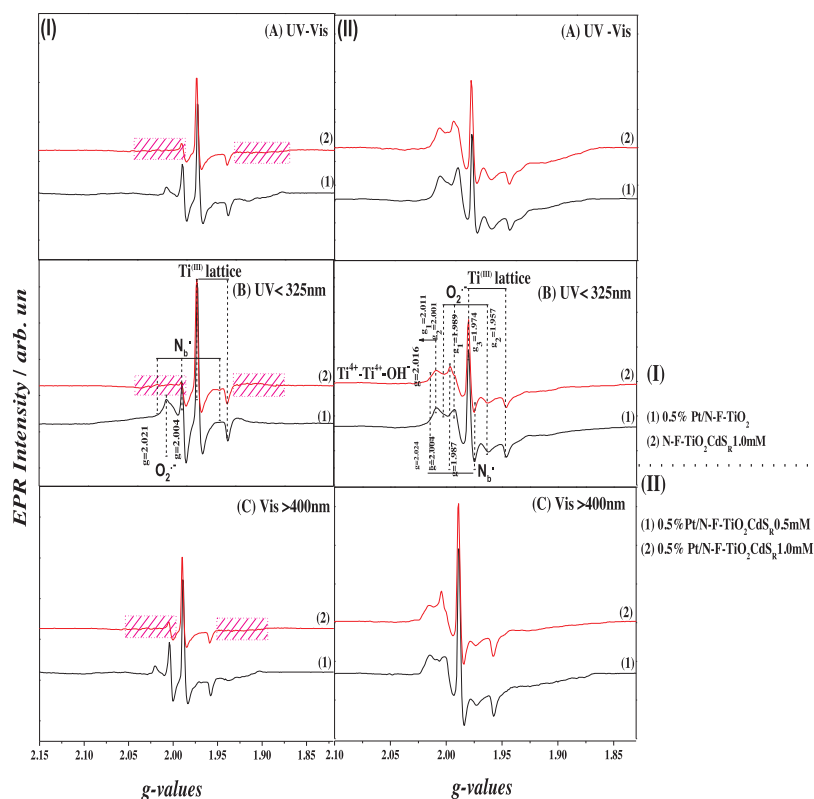As we can observe in Fig. 7 the best catalytic activity is obtained by

Fig. 6. EPR spectra (light minus dark) of **(I)** Pt/N-F-TiO$_2$CdS$_R$ and **(II)** Pt/N-F-TiO$_2$ & N-F-TiO$_2$CdS$_R$ 1 mM at 77 K. **(A)** UV–vis **(B)** UV λ < 325 nm, **(C)** Visible λ > 400 nm, light irradiation.

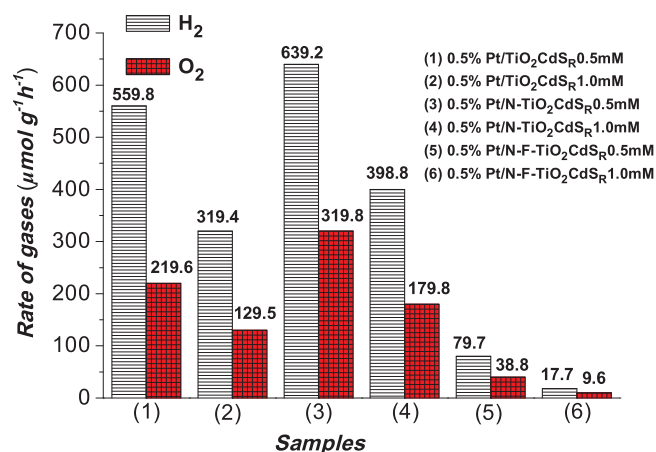**Fig. 7.** Column bars of evolved gases (μmol/g/h).

the Pt-TiO$_2$/N-CdS$_R$, which achieved a gas production rate of 639 μmol/g/h for H$_2$ and 319 μmol/g/h for O$_2$. These production rates declined on going towards undopped TiO$_2$, for all catalysts. Notice that, all the

hybrid catalysts with *lower* CdS$_R$ concentration (0.5 mM *vs* 1.0 mM) showed the highest activity (1.8, 1.6 and 4.4 times for the samples Pt/TiO$_2$-CdS$_R$, Pt/TiO$_2$/N-CdS$_R$ and Pt/TiO$_2$/N-F-CdS$_R$ respectively). F-codoping had a clear negative effect [47]: Pt-TiO$_2$/N/F-CdS$_R$ produced only 79.7 (17.7) μmol/g/h of H$_2$ gas for 0.5 mM (1 mM) CdS respectively (i.e 8 and 21 times lower *vs.* the homologous N-doped).

The better catalytic activity of the N- doped catalyst with the lower CdS$_R$ loading (0.1.mM) is attributed to acceleration of photoreduction mechanism in N-doped TiO$_2$ catalysts. As we have shown in our previous studies [21,31,32,39] the insertion of N anion in the lattice crystal of TiO$_2$, causes a lowering of conduction band of TiO$_2$ promoting e-donation capacity to participate in H$_2$-formation reactions. This is consistent with our EPR data (Figs. 5 and S2), which show that the incorporation of N in anatase lattice, creates additional photoexcited species (N$_b$˙) according to Eq. (3)

This contributes additional electrons to the conduction band. Also, the N–doping of TiO$_2$ promotes surface Ti$^{(III)}$ electrons (i.e. I$_{Tisurface}^{3+}$ (e$^-$) x 10^{-4} = 79 & 50 for Samples (3) & (4), *vs* I$_{Tisurface}^{3+}$ (e$^-$) x 10^{-4} = 74 & 35 for Samples (1) & (2), respectively). Thus, both these two e-sources accelerate the H$_2$ production rate in the conduction band of CdS$_R$ (Table 4, Fig S2 & paragraph 3.5). In contrast, in the case of N/F co-

Table 5
Comparison of H$_2$ evolution for different TiO$_2$ semiconductors.

Photocatalyst	Light Source	Sacrificial agent	Activity (μmol/ h/g)	Reference
Pt/HS-TiO$_2$	400 W Hg, > 420nm	Methanol	1023.71	[13]
Pt/N-TiO$_2$	300 W Xe > 400 nm	Methanol	125	[15]
3DOM TiO$_2$-Au-CdS	34 mW/cm^{2}UV & 158 mW/cm^2 visible, PLS-SXE-300C	Na$_2$S/ Na$_2$SO$_3$	1810	[16]
CdS/Au/N-TiO$_2$	750 W Xe, UV-Vis	Na$_2$S/ Na$_2$SO$_3$	100	[17]
Pt/CdS/TiO$_2$	500 W Hg–Xe arc lamp	glycerol	65	[18]
CdS/Pt-TiO$_2$	450 W Xe > 420nm	Na$_2$S/ Na$_2$SO$_3$	121.2	[20]
Pt-TiO$_2$/CdS	300 W Xe > 420nm	–	3.074	[22]
0.5%Pt-N-TiO$_2$CdS$_R$0.5 mM	125 W Hg > 290nm	–	639.2	This work

doped TiO_2, electrons are preferably localised as *lattice* Ti(III) e- at the expense of surface electrons disfavouring reduction of H^+ to H_2.

As we can observe from Table 5, the highest amount of H_2 production has been produced, in analogous systems, by a catalytic system CdS/(Pt-TiO_2) with 121.3 μmol/ h/g, using Na_2S/ Na_2SO_3 as redox mediator [20], while in similar case, the use of an artificial grill, as meaning for prevention of CdS photocorrosion, the H_2 amount was just 3.074 μmol/ h/g [22]. So far in the present work for the system 0.5%Pt-N-TiO_2CdS$_R$0.5 mM the total H_2 amount was 639.2 μmol/ h/g, indicating the beneficial role of N-Doping in the lattice of TiO_2.

Overall, the data in Fig. 7 and Table 5 show that: [i] CdS$_R$ is required for a high-photocatalytic water splitting efficiency. [ii] however high CdS$_R$ loading is inhibitory for the water splitting photocatalysis. [iii] N-doping of TiO_2 is beneficial for the photocatalytic performance of the CdS$_R$-loaded catalysts. Thus, our set of materials allow a better understanding of the role of CdS$_R$ together with N-doping in relation to their photocatalytic efficiency as well the chemical stability/corrosion of CdS$_R$. In the following we discuss in detail our data on CdS$_R$ corrosion, monitored via the Cd^{2+} ions' release by the materials during the water splitting catalysis. Then, a coherent mechanism is discussed taking into account the EPR photodynamics data.

3.7. CdS$_R$ photocorrositon

As soon as CdS$_R$ is photocorroded, Cd^{2+} ions are leaching in the solution. These Cd^{2+} ions are a quantitative index of the photocorrosion of CdS$_R$, which in turn has a negative impact on the photocatalytic performance at longer times. The analytical Cd-leaching tests, realized using Anodic Stripping Voltammetry (ASV) (Fig. 8) show that the Cd-leaching rate was significant i.e. 140 ppm of Cd^{2+} materials in **non**-N doped materials. Nitrogen doping of TiO_2 leads to ternary photocatalysts with decreasing photocorrosion i.e. 10 ppm of Cd^{2+}. Thus the present data show clearly, that N-doping has a beneficial effect on CdS$_R$ photocorrosion. This trend is corroborated by the water splitting results i.e. eliminating the inhibition of water splitting efficiency.

The lower catalytic activity of catalysts with higher CdS$_R$ loading is because of the higher amount of S° formed on the catalyst as a consequence of photo corrosion [48–50]. As we discuss hereafter, CdS$_R$ can be decomposed via two reactions i.e. due to the holes, (reaction (5)) or the photo generated O_2 (Reaction (6)):
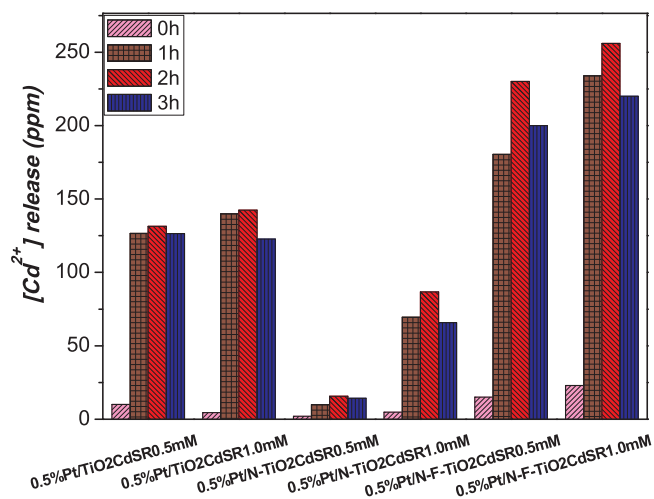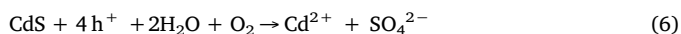
$$CdS + 2h^+ \rightarrow Cd^{2+} + S° \quad (5)$$

$$CdS + 4h^+ + 2H_2O + O_2 \rightarrow Cd^{2+} + SO_4^{2-} \quad (6)$$

Fig. 8. [Cd^{2+}] metal release by Pt/TiO_2CdS$_R$, Pt/N-TiO_2CdS$_R$ & Pt/N-F-TiO_2CdS$_R$ hybrid catalysts in water suspension, under photocatalytic reaction conditions.

Notice that photocorrosion is not only because of h^+ generation, but also is related with the produced O_2 from the photocatalytic splitting water. Reaction (6) is proven by our TGA data (Fig. S3), where a significant rate of mass *gain* was observed in the range of T = 400–580 °C, attributed to formation of $CdSO_4$, as a consequence of O_2 evolution [22].

The Cd^{2+} leaching due to photo-corrosion is correlated with the reusability of the catalysts. The data in Fig.S7 (**A**), show that the photocatalytic performance of the 0.5%Pt-N-TiO_2CdS$_R$0.5 mM catalyst can be retained for up to 3-reuses. The XRD data of the reused 0.5%Pt-N-TiO_2CdS$_R$0.5 mM catalyst show that no-structural changes are detected by XRD in the reused catalyst Fig.S7 (**B**). It is confirmed that the deactivation is coming from photocorrosion and not from change in the morphology of the catalyst. Instead, the present Cd^{2+}-leaching data provide a sensitive index of the underlying mechanism of CdS photo corrosion which -via formation of $CdSO_4$-drives the deactivation of the photocatalysts.

3.8. Mechanistic insights

3.8.1. N-doping inhibits CdS$_R$ photocorrosion

The beneficial effect of N-doping on the acceleration of catalytic activity of TiO_2 has been well documented in the literature [15,17,21]. However the stabilizing effect on N-doping *vs.* CdS$_R$ photocorrosion, has not been discussed previously and must be attributed in the photocatalytic mechanism operating in CdS$_R$/Pt-N-TiO_2 ternary photocatalysts.

We consider that the higher stabilization of CdS particles on the surface of Pt-N-TiO_2 photocatalysts is due to the higher amount of surface electrons formed in such photocatalysts *via* the mechanism described in reaction (2). On the other hand, as shown previously [21,31] in N/F co-doped TiO_2, the Fluorine – as the most electronegative element – when incorporated in TiO_2 is trapping surface photo-generated electrons. Moreover, in N/F co-doped TiO_2, F ions drive N ions deeper in the lattice and forces creation of lattice Ti^{3+} ions at the expense of surface electrons, as shown herein by our EPR data [21,31].

Thus, N-atoms in ternary CdS$_R$/Pt-N-TiO_2 photocatalysts are suggested to accelerate water splitting rates and prevent photocorrosion while F anions embedded in CdS$_R$/Pt-N,F-TiO_2 photocatalysts, retards water splitting reaction. The proposed [retarded CdS photocorrosion] mechanism *via* the excess photoexcited surface electrons in CdS$_R$/Pt-N-TiO_2, is in accordance with the mechanism proposed by Tang *et al.* [23]. These authors [23] have developed an artful graphene sheltering Reduced Graphene Oxide (RGO) onto a TiO_2-nanotube (NT) array (RGO/CdSTiO_2 -NT) which showed an inhibition of CdS photocorrosion. They found that the RGO layer provides protection to CdS by offering an electron-rich microenvironment where the stored electrons on RGO(e⁻) not only reduce intermediate species S·- to S^{2-} but also compensate the valence band of CdS for its loss of electrons, alleviating CdS$_R$ photocorrosion from oxidation by holes [23]. Also, Tata *et al.* [48] have demonstrated that core-shell CdS/Au/TiO_2 can show enhanced endurance to photocorrosion *via* protection of CdS In an analogous manner, herein -based on EPR data- we suggest that N-doping in TiO_2 offers a reducing interfacial environment for the CdS$_R$, thus retarding photocorrosion.

3.8.2. A photocatalytic mechanism

Based on our data, a consistent photocatalytic mechanism is illustrated in Fig. 9. The energy positions for CB and VB have been estimated as described in Table S1.

From EPR spectroscopy and catalytic H_2/O_2 production results we can conclude that:

[a] in both N-doped as well as in N/F-codoped catalysts a Z-Scheme route [8,12,16,17] is operative. In all cases, a photoexcitation of TiO_2 electrons occurs, as a consequence of hv > Eg$_{TiO2}$ (3.2 eV → CdS$_R$/Pt-TiO_2, 2.9 eV → CdS$_R$/Pt-N-TiO_2, 2.7 eV → CdS$_R$/Pt-N-F-TiO_2), from the
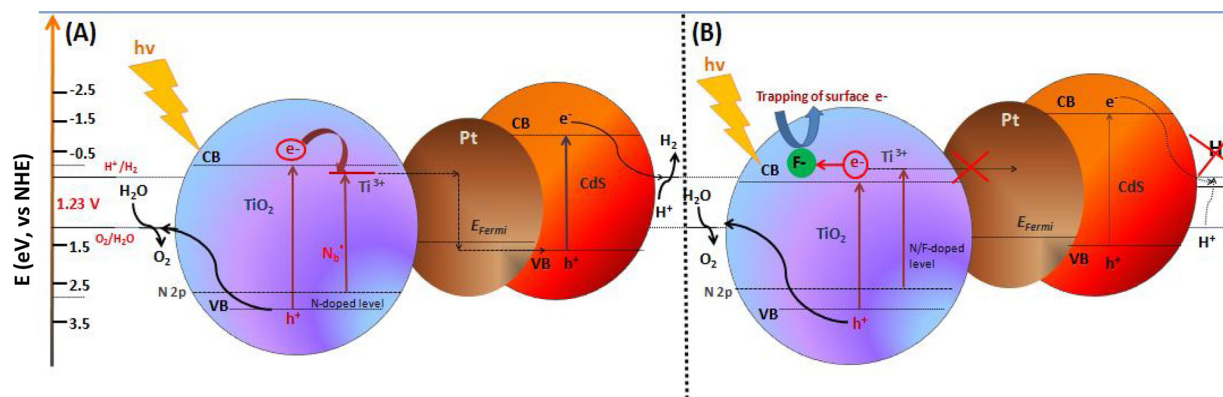
Fig. 9. Illustration of photocatalytic mechanism for **(a)** Pt/N-TiO$_2$CdS$_R$ & **(b)** Pt/N-F-TiO$_2$CdS$_R$ hybrid catalysts.

valence band (VB) to the conduction band (CB). As the E$_{fermi}$ of Pt metal is 1.5 eV NHE [51], the photoexcited e$^-$ should overcome this minimum energy on` the vacuum (- 6 eV). As the Pt act as a mediator of electron transfer process, the E$_{fermi}$ is determinant for all catalytic process. The excited electrons from the CB of TiO$_2$ can flow from the Pt metal states to the VB of CdS$_R$, therefore the h$^+$ of TiO$_2$ is available for oxidation of H$_2$O to O$_2$. The h$^+$ from the VB of CdS$_R$ is flowing into the Pt states to recombine with the stored electrons, as long as the E$_{fermi}$ of Pt is higher that VB value of CdS$_R$ (+ 2.1 eV vs NHE) [45]. Thus the electrons of CdS$_R$ are available for reduction of H$^+$ to H$_2$.

In the case of Nitrogen doping, the insertion of N-atom into the lattice, results in intraband-gap states [21], thus lowering of CB of TiO$_2$. This favors promotion of the photoexcited electrons in into the Pt° energy levels. The stored electrons create a reducing interfacial environment in CdS$_R$/Pt-N- TiO$_2$, thus inhibiting the oxidation of CdS$_R$, because of the higher capacity of h$^+$ of CdS$_R$ to recombine with the electrons stored into the Pt° metal. F$^-$ anion codoping with N, contributes to the suppression of e- storage on Pt° as a consequence of :[i] insertion of N atom to the TiO$_2$ lattice, disfavoring flow of electrons to the Pt° particles, [ii] as it was shown previously by our group [21,31] and the present EPR data, it is clear that the F- anion acts as a surface electron scavenger. The positive synergism between N-doping and CdS$_R$ stabilisation, revealed in the present work, bears relevance to other observations on the stabilisation/photocatalytic efficiency enhancement by pertinent Z-scheme photocatalsysts [19,48]. Herein, it is further demonstrated that N *vs.* N/F doped TiO$_2$, can also have a decisive impact on the CdS stabilisation mechanism, as a consequence of the atomic details of localisation of N and the balance of surface *vs.* lattice electrons.

4. Conclusions

The photocatalytic H$_2$/O$_2$ production data show that N-incorporation in the TiO$_2$ lattice boosts overall water splitting, while F-incoprotration inhibits the catalytic performance. The 0.5CdS$_R$/Pt-N-TiO$_2$ material achieved a photocatlytic production of 639μmoles/gr/h of H$_2$ in tandem with 319μmoles/gr/h of O$_2$. Quantitative monitoring of the photogenerated Ti^{3+}-surface and Ti^{3+}-lattice electrons, as well as of the photgnereated holes (h$^+$) by Electron Parmagnetic Resonce spectrsocopy show that the CdS/Pt-N-TiO$_2$ achieves enhanced e$^-$/h$^+$ photogeneration due to intraband states generated by N-dopping, facilitating the flow of electrons *via* Pt to the valence band of CdS. A dual beneficial role of N-atoms, boosting the visible light photocactivity and inhibiting CdS photocorrosoion is documented. A consistent Z-scheme reaction mechanism is proposed for the catalytic H$_2$ production by CdS/Pt-N-TiO$_2$ and CdS/Pt-N-F-TiO$_2$ heterojunctions, taking into account the photoinduced e$^-$/h$^+$ dynamics as well as the interfacial {CdS} /{Pt-N/F-TiO$_2$} chemistry.

Appendix A. Supplementary data

Supplementary material related to this article can be found, in the online version, at doi:https://doi.org/10.1016/j.apcatb.2019.04.091.

References

[1] A. Fujishima, K. Honda, Electrochemical photolysis of water at a semiconductor electrode, Nature. 238 (1972) 37–38, https://doi.org/10.1038/238037a0.

[2] X. Chen, S. Shen, L. Guo, S.S. Mao, Semiconductor-based photocatalytic hydrogen generation, Chem. Rev. (Washington DC, U.S.) 110 (2010) 6503–6570, https://doi.org/10.1021/cr1001645.

[3] M.G. Walter, E.L. Warren, J.R. McKone, S.W. Boettcher, Q. Mi, E.A. Santori, N.S. Lewis, Solar Water splitting cells, Chem. Rev. (Washington, DC, U.S.) 110 (2010) 6446–6473, https://doi.org/10.1021/cr1002326.

[4] R.M. Navarro Yerga, M. Consuelo Álvarez Galván, F. del Valle, J.A. Villoria de la Mano, J.L.G. Fierro, Water splitting on semiconductor catalysts under visible light irradiation, ChemSusChem. 2 (2009) 471–485, https://doi.org/10.1002/cssc.200900018.

[5] S.E. Salas, B.S. Rosales, H. Lasa, Quantum yield with platinum modified TiO2 photocatalyst for hydrogen production, Appl. Catal. B Environ. 140–141 (2013) 523–536, https://doi.org/10.1016/j.apcatb.2013.04.016.

[6] J. Li, M.W.G. Hoffmann, H. Shen, C. Fabrega, J.D. Prades, T. Andreu, F. Hernandez-Ramirez, S. Mathur, Enhanced photoelectrochemical activity of an excitonic staircase in CdS@TiO2 and CdS@anatase@rutile TiO2 heterostructures, J Mater. Chem. 22 (2012) 20472–20476, https://doi.org/10.1039/c2jm33404f.

[7] M. Shen, Z. Yan, L. Yang, P. Du, J. Zhang, B. Xiang, MoS2 nanosheet/TiO2 nanowire hybrid nanostructures for enhanced visible-light photocatalytic activities, Chem. Commun. 50 (2014) 15447–15449, https://doi.org/10.1039/C4CC07351G.

[8] A. Manivannan, N. Wu, Solar hydrogen generation by a CdS-Au-TiO2 Sandwich nanorod array enhanced with Au nanoparticle as electron relay and plasmonic photosensitizer, J. Am. Chem. Soc. 136 (2014) 8438–8449, https://doi.org/10.1021/ja503508g.

[9] W.Y. Teoh, L. Mädler, R. Amal, Inter-relationship between Pt oxidation states on TiO2 and the photocatalytic mineralisation of organic matters, J Catal. 251 (2007) 271–280, https://doi.org/10.1016/j.jcat.2007.08.008.

[10] A. Naldoni, M. D'Arienzo, M. Altomare, M. Marelli, R. Scotti, F. Morazzoni, E. Selli, V. Dal Santo, Pt and Au/TiO2 photocatalysts for methanol reforming: role of metal nanoparticles in tuning charge trapping properties and photoefficiency, Appl. Catal. B Environ. 130–131 (2013) 239–248, https://doi.org/10.1016/j.apcatb.2012.11.006.

[11] T. Hirakawa, P.V. Kamat, V. Uni, N. Dame, Charge separation and catalytic activity of Ag @ TiO 2 core-shell composite clusters under UV-irradiation, J Am. Chem. Soc.

127 (2005) 3928–3934, https://doi.org/10.1021/ja042925a.

[12] Y. Deligiannakis, Nanomaterials for environmental solar energy technologies: applications & limitations, Kona Powder Part. J 35 (2018) 14–31, https://doi.org/10.14356/kona.2018004.

[13] Z. Zhu, C.T. Kao, B.H. Tang, W.C. Chang, R.J. Wu, Efficient hydrogen production by photocatalytic water-splitting using Pt-doped TiO2 hollow spheres under visible light, Ceram. Int. 42 (2015) 6749–6754, https://doi.org/10.1016/j.ceramint.2016.01.047.

[14] Y.Z. Yang, C.H. Chang, H. Idriss, Photo-catalytic production of hydrogen form ethanol over M/TiO2 catalysts (M = Pd, Pt or Rh), Appl. Catal. B Environ. 67 (2006) 217–222, https://doi.org/10.1016/j.apcatb.2006.05.007.

[15] T. Sreethawong, S. Laehsalee, S. Chavadej, Use of Pt/N-doped mesoporous-as-sembled nanocrystalline TiO2 for photocatalytic H2 production under visible light irradiation, Catal. Commun. 10 (2009) 538–543, https://doi.org/10.1016/j.catcom.2008.10.029.

[16] H. Zhao, M. Wu, J. Liu, Z. Deng, Y. Li, B.L. Su, Synergistic promotion of solar-driven H2 generation by three-dimensionally ordered macroporous structured TiO2-Au-CdS ternary photocatalyst, Appl. Catal. B Environ. 184 (2016) 182–190, https://doi.org/10.1016/j.apcatb.2015.11.018.

[17] H. Zhou, L. Ding, T. Fan, J. Ding, D. Zhang, Q. Guo, Leaf-inspired hierarchical porous CdS/Au/N-TiO2 heterostructures for visible light photocatalytic hydrogen evolution, Appl. Catal. B Environ. 147 (2014) 221–228, https://doi.org/10.1016/j.apcatb.2013.08.025.

[18] M. De Oliveira Melo, L.A. Silva, Visible light-induced hydrogen production from glycerol aqueous solution on hybrid Pt-CdS-TiO2 photocatalysts, J Photochem. Photobiol. A Chem. 226 (2011) 36–41, https://doi.org/10.1016/j.jphotochem.2011.10.012.

[19] H. Park, W. Choi, M.R. Hoffmann, Effects of the preparation method of the ternary CdS/TiO2/Pt hybrid photocatalysts on visible light-induced hydrogen production, J Mater. Chem. 18 (2008) 2379, https://doi.org/10.1039/b718759a.

[20] H. Park, Y.K. Kim, W. Choi, Reversing CdS preparation order and its effects on photocatalytic hydrogen production of CdS / Pt-TiO2 hybrids under visible light, J Phys. Chem. C. 115 (2011) 6141–6148, https://doi.org/10.1021/jp2015319.

[21] A.E. Giannakas, M. Antonopoulou, J. Papavasiliou, Y. Deligiannakis, I. Konstantinou, Photocatalytic performance of Pt-TiO 2, Pt-N-TiO 2 and Pt-N/F-TiO 2 towards simultaneous Cr(VI) reduction/benzoic acid oxidation: insights into photogenerated charge carrier dynamics and catalyst properties, J Photochem. Photobiol A Chem. 349 (2017) 25–35, https://doi.org/10.1016/j.jphotochem.2017.08.066.

[22] X. Ning, J. Li, B. Yang, W. Zhen, Z. Li, B. Tian, G. Lu, Inhibition of photocorrosion of CdS via assembling with thin film TiO2 and removing formed oxygen by artificial gill for visible light overall water splitting, Appl. Catal. B Environ. 212 (2017) 129–139, https://doi.org/10.1016/j.apcatb.2017.04.074.

[23] Y. Tang, X. Hu, C. Liu, Perfect inhibition of CdS photocorrosion by graphene sheltering engineering on TiO2 nanotube array for highly stable photocatalytic activity, Phys. Chem. Chem. Phys. 16 (2014) 25321–25329, https://doi.org/10.1039/c4cp04057k.

[24] I.T. Papadas, C. Kosma, Y. Deligiannakis, Ternary [Al2O3–electrolyte–Cu2+] species: EPR spectroscopy and surface complexation modeling, J. Colloid Interface Sci. 339 (2009) 19–30, https://doi.org/10.1016/j.jcis.2009.07.008.

[25] Y. Georgiou, E. Mouzourakis, A.B. Bourlinos, R. Zboril, M.A. Karakassides, A.P. Douvalis, Th. Bakas, Y. Deligiannakis, Surface decoration of amine-rich carbon nitride with iron nanoparticles for arsenite (AsIII) uptake: The evolution of the Fe-phases under ambient conditions, J. Hazard. Mater. 312 (2016) 243–253, https://doi.org/10.1016/j.jhazmat.2016.03.066.

[26] H. Rietveld, Line profiles of neutron powder-diffraction peaks for structure refinement, Acta Crystallogr. 22 (1967) 151–152, https://doi.org/10.1107/S0365110X67000234.

[27] T.T.D. Vu, F. Mighri, A. Ajji, T.-O. Do, Synthesis of titanium dioxide/cadmium sulfide nanosphere particles for photocatalyst applications, Ind. Eng. Chem. Res. 53 (2014) 3888–3897, https://doi.org/10.1021/ie403718n.

[28] N. Bao, L. Shen, T. Takata, K. Domen, Self-templated synthesis of nanoporous CdS nanostructures for highly efficient photocatalytic hydrogen production under visible light, Chem. Mater. 20 (2008) 110–117, https://doi.org/10.1021/cm7029344.

[29] W. Kim, T. Tachikawa, H. Kim, N. Lakshminarasimhan, P. Murugan, H. Park, T. Majima, W. Choi, Visible light photocatalytic activities of nitrogen and platinum-doped TiO2: synergistic effects of co-dopants, Appl. Catal. B: Environ. 147 (2014) 642–650, https://doi.org/10.1016/j.apcatb.2013.09.034.

[30] G. Yang, T. Wang, B. Yang, Z. Yan, S. Ding, T. Xiao, Enhanced visible-light activity of F-N co-doped TiO2 nanocrystals via nonmetal impurity, Ti3+ ions and oxygen vacancies, Appl. Surf. Sci. 287 (2013) 135–142, https://doi.org/10.1016/j.apsusc.2013.09.094.

[31] A.E. Giannakas, E. Seristatidou, Y. Deligiannakis, I. Konstantinou, Photocatalytic activity of N-doped and N-F co-doped TiO2 and reduction of chromium(VI) in

aqueous solution: an EPR study, Appl. Catal. B Environ. (2013) 132–133, https://doi.org/10.1016/j.apcatb.2012.12.017.

[32] A.E. Giannakas, M. Antonopoulou, C. Daikopoulos, Y. Deligiannakis, I. Konstantinou, Characterization and catalytic performance of B-doped, B-N co-doped and B-N-F tri-doped TiO2 towards simultaneous Cr(VI) reduction and benzoic acid oxidation, Appl. Catal. B Environ. 184 (2016), https://doi.org/10.1016/j.apcatb.2015.11.009.

[33] S. Hashimoto, A. Tanaka, Alteration of Ti 2p XPS spectrum for titanium oxide by low-energy Ar ion bombardment, Surf. Interface Analysis 34 (2002) 262–265, https://doi.org/10.1002/sia.1296.

[34] A.A. Rempel, E.A. Kozlova, T.I. Gorbunova, S.V. Cherepanova, E.Y. Gerasimov, N.S. Kozhevnikova, A.A. Valeeva, E.Y. Korovin, V.V. Kaichev, Y.A. Shchipunov, Synthesis and solar light catalytic properties of titania–cadmium sulfide hybrid nanostructures, Catal. Commun. 68 (2015) 61–66, https://doi.org/10.1016/j.catcom.2015.04.034.

[35] N. Kakuta, J.M. White, A. Campion, A.J. Bard, M.A. Fox, S.E. Webber, Surface analysis of semiconductor-incorporated polymer systems. 1. nafion and cadmium sulfide-nafion, J. Phys. Chem. 89 (1985) 48–52, https://doi.org/10.1021/j100247a014.

[36] B. Bharti, S. Kumar, H.-N. Lee, R. Kumar, Formation of oxygen vacancies and Ti3 + state in TiO2 thin film and enhanced optical properties by air plasma treatment, Sci. Rep. 6 (2016), https://doi.org/10.1038/srep32355.

[37] C.D. Wagner, D.A. Zatko, R.H. Raymond, Use of the oxygen KLL Auger lines in identification of surface chemical states by electron spectroscopy for chemical analysis, Anal. Chem. 52 (1980) 1445–1451, https://doi.org/10.1021/ac50059a017.

[38] Z. Ai, G. Zhao, Y. Zhong, Y. Shao, B. Huang, Y. Wu, X. Hao, Phase junction CdS: high efficient and stable photocatalyst for hydrogen generation, Appl. Catal. B Environ. 221 (2018) 179–186, https://doi.org/10.1016/j.apcatb.2017.09.002.

[39] A.E. Giannakas, M. Antonopoulou, Y. Deligiannakis, I. Konstantinou, Preparation, characterization of N-I co-doped TiO2 and catalytic performance toward simultaneous Cr(VI) reduction and benzoic acid oxidation, Appl. Catal. B Environ. (2013) 140–141, https://doi.org/10.1016/j.apcatb.2013.04.052.

[40] C.P. Kumar, N.O. Gopal, T.C. Wang, EPR investigation of TiO2 nanoparticles with temperature-dependent properties, J. Phys. Chem. B 110 (2006) 5223–5229, https://doi.org/10.1021/jp057053t.

[41] Y. Nakaoka, Y. Nosaka, ESR investigation into the effects of heat treatment and crystal structure on radicals produced over irradiated TiO2 powder, J. Photochem. Photobiol. A Chem. 110 (1997) 299–305, https://doi.org/10.1016/S1010-6030(97)00208-6.

[42] S.W. Ahn, K.H. Kang, D. Il Hong, Photoionization of TiO2 particles incorporated into silica gels studied by EPR spectroscopy, J. Korean Soc. Magn. Reson. Med. 4 (2000) 50–63.

[43] C. Di Valentin, E. Finazzi, G. Pacchioni, A. Selloni, S. Livraghi, A.M. Czoska, M.C. Paganini, E. Giamello, Density functional theory and electron paramagnetic resonance study on the effect of N−F codoping of TiO 2, Chem. Mater. 20 (2008) 3706–3714, https://doi.org/10.1021/cm703636s.

[44] S. Livraghi, M.C. Paganini, E. Giamello, A. Selloni, C. Di Valentin, G. Pacchioni, Origin of photoactivity of nitrogen-doped titanium dioxide under visible light origin of photoactivity of nitrogen-doped titanium dioxide under visible light, J. Am. Chem. Soc. 128 (2006) 15666–15671, https://doi.org/10.1021/ja064164c.

[45] G. Barolo, S. Livraghi, M. Chiesa, M.C. Paganini, E. Giamello, D. Chimica, U. Torino, V.P. Giuria, I. Torino, Mechanism of the photoactivity under visible light of N-doped titanium dioxide. Charge carriers migration in irradiated N-TiO 2 investigated by electron paramagnetic resonance, J. Phys. Chem. C 116 (2012) 20887–20894, https://doi.org/10.1021/jp306123d.

[46] A. Kudo, Y. Miseki, Heterogeneous photocatalyst materials for water splitting, Chem. Soc. Rev. 38 (2009) 253–278, https://doi.org/10.1039/B800489G.

[47] J. Yu, W. Wang, B. Cheng, B.L. Su, Enhancement of photocatalytic activity of mesoporous TiO2 powders by hydrothermal surface fluorination treatment, J Phys. Chem. C 113 (2009) 6743–6750, https://doi.org/10.1021/jp900136q.

[48] H. Tada, T. Mitsui, T. Kiyonaga, T. Akita, K. Tanaka, All-solid-state Z-scheme in CdS-Au-TiO2 three-component nanojunction system, Nat. Mater. 5 (2006) 782–786, https://doi.org/10.1038/nmat1734.

[49] A. Didden, P. Hillebrand, B. Dam, R. van de Krol, Photocorrosion mechanism of TiO 2 -coated photoanodes, Int. J. Photoenergy 2015 (2015) 1–8, https://doi.org/10.1155/2015/457980.

[50] W. Zhen, X. Ning, B. Yang, Y. Wu, Z. Li, G. Lu, The enhancement of CdS photocatalytic activity for water splitting via anti-photocorrosion by coating Ni2P shell and removing nascent formed oxygen with artificial gill, Appl. Catal. B Environ. 221 (2018) 243–257, https://doi.org/10.1016/j.apcatb.2017.09.02.

[51] S. Halas, T. Durakiewicz, Work functions of elements expressed in terms of the fermi energy and the density of free electrons, J. Phys. Condens. Matter. 10 (1999) 10815–10826, https://doi.org/10.1088/0953-8984/10/48/005.